Surfaces and Interfaces 87 (2026) 108989

Contents lists available at ScienceDirect

Surfaces and Interfaces

journal homepage: www.sciencedirect.com/journal/surfaces-and-interfaces

Gaining insight into the synthesis of nanosized pure zeolite NaA

Lucas Güemes [a,b], Joaquín Coronas [a,b], Carlos Téllez [a,b,*]

[a] Instituto de Nanociencia y Materiales de Aragón (INMA), Universidad de Zaragoza-CSIC, 50018 Zaragoza, Spain
[b] Departamento de Ingeniería Química y Tecnologías del Medio Ambiente, Universidad de Zaragoza, 50018 Zaragoza, Spain

ARTICLE INFO

Keywords:
Zeolite A
LTA type structure
Hydrothermal synthesis
Particle size
Morphology

ABSTRACT

In zeolite synthesis, controlling and reducing the particle size is advantageous for different processes in which mass transfer occurs through surface active sites. In this work, the hydrothermal synthesis of zeolite NaA has been studied in detail seeking to control the size, morphology and crystal phase of the resulting zeolite particles. Adjusting the crystallization conditions and molar composition of a SiO_2-Al_2O_3-TMA_2O-Na_2O-H_2O system allows for the consistent production of zeolite NaA with a particle size down to 68 nm measured by TEM, using tetramethylammonium (TMA) as the organic structure directing agent (OSDA). Within the composition region in which the LTA zeolite crystallization is favored, syntheses at higher OSDA/Na^+ and Si/Al atomic ratios produce smaller particles. Depending on the synthesis gel molar formulation, different morphologies and sizes of LTA crystals (in the ~68–760 nm range) with slightly distinct Si/Al atomic ratios (in the 1.1–2.3 range) can be achieved. The synthesized zeolites were characterized in detail by different techniques, and their textural properties were evaluated through CO_2 and N_2 adsorption and correlated with their composition.

1. Introduction

Zeolites are generally crystalline hydrated microporous aluminosilicates composed of TO_4 tetrahedra (T = Si, Al), in which each aluminum accounts for a structural negative charge that is balanced by the presence of extraframework cations. These cations are typically inorganic and can be exchangeable, giving rise to a rich ion-exchange chemistry. In fact, relying on their ion-exchange properties, zeolites have been extensively used in the formulation of laundry compositions as water softeners [1–3], which was their first industrial breakthrough [4]. Zeolite crystals are characterized by their rigid and ordered porous systems that allow only certain molecules to enter within the framework. Thus, the term molecular sieve was applied to zeolites [5], which, combined with the presence of catalytically active sites within the framework, constitute an unparalleled family of shape and size-selective adsorbents and catalysts [6].

Many zeolites occur naturally as minerals, stilbite being discovered and termed as the first zeolite by A.F. Cronstedt in 1756 [7], but synthetic zeolites have attracted greater attention. H.E. Sainte-Claire Deville reported the first hydrothermal synthesis of zeolite levynite in 1862 [8]. Nevertheless, zeolite synthesis science started to bloom in the 1940s. The investigations carried out by Prof. R.M. Barrer in the 1940s, regarding the large-scale production of different zeolites [9], established the foundation for zeolite research in the next decades [10]. New unprecedented synthetic zeolites were obtained, followed by several patent applications. R.M. Milton and D.W. Breck at Union Carbide discovered, studied and stated synthesis procedures for zeolites A, X and Y [11], achieving remarkable success in adsorption and separation processes. Later, the commercialization of the synthetic ultrastable Y zeolite (USY) in the fluid catalytic cracking (FCC) process transformed the oil refinery industry [6]. More examples of zeolite advances came with the introduction of quaternary ammonium cations, which allowed to direct zeolite synthesis to obtain more siliceous zeotypes [12]. Also, the isomorphic substitution of Si and Al with other elements resulted in the development of new materials, such as aluminophosphates (AlPOs), which have alternating AlO_4^- and PO_4^+ entities, constituting nonsilicon zeolitic frameworks named as pseudozeolites [13].

To date, the International Zeolite Association (IZA) has reported >260 zeolitic framework types [14]. Among all zeolites, zeolite A, which is considered as the reference material for the Linde Type A (LTA) framework, stands out due to its high commercial and academic importance. Zeolite A is grouped as a small pore zeolite given the size of their 8-membered ring pore apertures, which are ~3 Å, 4 Å or 5 Å depending on whether the extraframework cations are K^+, Na^+ or Ca^{2+}, respectively. In comparison with other zeolites, zeolite A can incorporate the highest zeolitic aluminum content allowed by the Löwenstein's

* Corresponding author at: Instituto de Nanociencia y Materiales de Aragón (INMA), Universidad de Zaragoza-CSIC, 50018 Zaragoza, Spain.
E-mail address: ctellez@unizar.es (C. Téllez).

https://doi.org/10.1016/j.surfin.2026.108989
Received 23 December 2025; Received in revised form 10 March 2026; Accepted 11 March 2026
Available online 12 March 2026

rule [15], which turns into a high content of extraframework cations to maintain the charge neutrality. These cations can be exchangeable, which made zeolite A replace phosphates as sustainable (not contributing to eutrophication) water softeners [16]. In fact, this exchange property has also opened the door to prepare antimicrobial materials by exchanging zeolite A with silver ions [17]. The charge dispersion among the negatively charged zeolite framework and the presence of extraframework cations make zeolite A highly hydrophilic, which explains its use in drying gas and liquid streams [4]. Moreover, it also shows affinity for other species, such as CO_2, through the formation of electrostatic interactions [18].

Regarding the synthesis of zeolites, the precise control and reduction of particle size could be advantageous, as a lower particle size would enhance any process in which mass transfer occurs through surface active sites, as adsorption related processes. An interesting case study appears with membranes for separation processes. Given the transport properties and separation capability of zeolite NaA [18], its use as a filler for mixed matrix membrane fabrication has been explored. Achieving a stable dispersion of zeolite crystals is required to avoid phase segregation during membrane fabrication; for this purpose, nanosized zeolites are better candidates than larger particles. Moreover, the transition from dense membranes to thin-film nanocomposite membranes, which would allow for higher flux processing, necessitates particles of reduced size. Another potential application for LTA zeolites lies in the field of catalysis, in which tuning the Si/Al ratio and particle size of zeolite crystals has been shown to be fundamental [17,19]. In any case, the precise control over zeolite A synthesis (e.g., size, morphology or Si/Al ratio) is of major importance for its commercial application.

Although there are different techniques to produce zeolites, the hydrothermal method has been established as the basic synthetic route [20]. Under hydrothermal conditions, it is possible to dissolve and recrystallize materials that are insoluble under normal conditions [21]. Nevertheless, the chemistry behind zeolite synthesis is complex. Zeolite crystallization involves different bidirectional reactions, such as dissolution-precipitation, polymerization-depolymerization, and nucleation-crystallization steps. In fact, these processes allow the obtaining of a crystalline material from an amorphous intermediate one. Regarding zeolite A, there are several studies in which zeolite A is crystallized employing TMAOH, as organic structure directing agent (OSDA) to produce nanosized zeolite A (**Table S1**) [22–32]. Most of the studies cited in **Table S1** focus on a fundamental point of view, lacking the existing relationships between the composition, particle size, and morphology of the zeolite NaA batch synthesis and its correlation with the resulting adsorption properties.

In this work, we systematically study the hydrothermal synthesis of batch zeolite A employing TMAOH as OSDA and analyze in detail the properties of the resulting zeolites. Different parameters including synthesis gel composition, crystallization conditions and aging time are evaluated, aiming to produce nanosized zeolite NaA. The obtained crystalline phases are analyzed by PXRD, revealing the region in which the LTA structure forms. The different morphologies and particle size distributions of the obtained LTA zeolites are assessed by SEM and TEM, proving their correlation with the synthesis conditions. The textural properties of the resulting zeolites are evaluated in detail through CO_2 and N_2 adsorption and associated with the synthesis starting gel composition. Moreover, DLS provides complementary information regarding the size distributions and hydrophilic character of the different syntheses. Herein, we provide valuable insights concerning the OSDA based synthesis of zeolite A.

2. Experimental section

2.1. Materials

Colloidal silica (Ludox®, 40 wt. % suspension in H_2O) and sodium chloride (NaCl, 99 %) were purchased from Sigma Aldrich. Aluminum isopropoxide (AlP, 98 %) was acquired in powder form from Acros Organics, sodium hydroxide micropearls (NaOH, 99 %) were obtained from Glentham Life Sciences, and tetramethylammonium hydroxide pentahydrate (TMAOH, 97 %) was received from Indagoo. Any use of water reported for the zeolite synthesis gel preparation corresponds to milli-Q H_2O, obtained from a Millipore device, while H_2O for synthesis washing was obtained from Productos Gilca S.C.

2.2. Synthesis of zeolite A

2.2.1. Synthesis gel preparation

Zeolite syntheses were carried out following the scheme presented in Fig. 1. Initially, TMAOH was dissolved in a polypropylene (PP) bottle with ultrapure H_2O, to which a specific volume of a prepared 5 M NaOH aqueous solution was added. The PP bottle content was divided into two equal volumes, aluminum isopropoxide was added to one of the PP bottles while colloidal silica was added to the other. The two solutions were stirred until becoming transparent and, subsequently, the silicate solution was poured immediately into the aluminate solution while continuously stirring. Gel syntheses were further stirred for 5 min, and then transferred to an orbital stirring plate for aging at room temperature (RT) for 72 h. The specific amounts of reagents were calculated for each experiment following the desired synthesis gel molar composition: $a$$SiO_2$, $b$$Al_2O_3$, $c$$H_2O$, $d$$TMA_2O$ and $e$$Na_2O$.

2.2.2. Hydrothermal synthesis

The aged synthesis gels were transferred into a Teflon-lined stainless-steel autoclave and hydrothermally treated in a preheated oven at 100 °C for 12 h. The oven was equipped with a rotating plate (at ca. 30 rpm) that allowed continuously stirring the zeolite precursor gels. After the hydrothermal synthesis, crystallization was quenched by immersing the autoclaves into an ice-water bath. The same Teflon vessels were employed for all the syntheses and in between experiments, they were washed with NaOH ~10 M at 150 °C.

After the hydrothermal treatment, solid zeolites were centrifuged and washed several times with H_2O until pH~9–10. The resultant slurries were dried at 90 °C and finally calcined at 500 °C for 4 h (1 °C·min^{-1}).

2.3. Characterization

2.3.1. Powder X-ray diffraction

The powder X-ray diffraction (PXRD) patterns of the calcined zeolites were collected in a PANalytical Empyrean-Multipurpose diffractometer (CuK_α λ = 1.54060 Å, 40 mA, 45 kV) employing a reflection-transmission spinner stage with a zero-background sample holder. The diffraction patterns were acquired in Bragg-Brentano configuration, in the range of 2θ = 5–40°. The profile fitting was performed with X'Pert HighScore Plus version 3.0 software.

2.3.2. Field-emission scanning and transmission electron microscopy

Field-emission scanning electron microscopy (FE-SEM) images of the zeolites were acquired in an Inspect F50 model (FEI, operated at 10 kV) coupled with an energy-dispersive X-ray (EDX) detector that allowed to quantify the zeolite chemical composition, as the Si to Al ratios. In all cases, a zeolite slurry drop was deposited onto carbon tape and left until it was completely evaporated. Then, samples were coated with Pd. From the zeolite SEM images, 500 size measurements of the unequivocally particle edges were taken with ImageJ software version 1.54 g to construct the particle size distributions (PSD) in which the y-axis (not shown) corresponds to the frequency of data points within each bin. Transmission electron microscopy (TEM) images were obtained using a Tecnai T20 microscope (Thermo Fisher Scientific) operated at 200 kV. For TEM images, a drop of zeolite powder dispersed in water was placed onto a carbon coated 300 mesh copper grid. In the case of zeolite synthesis with smaller particle sizes, TEM provided higher-resolution

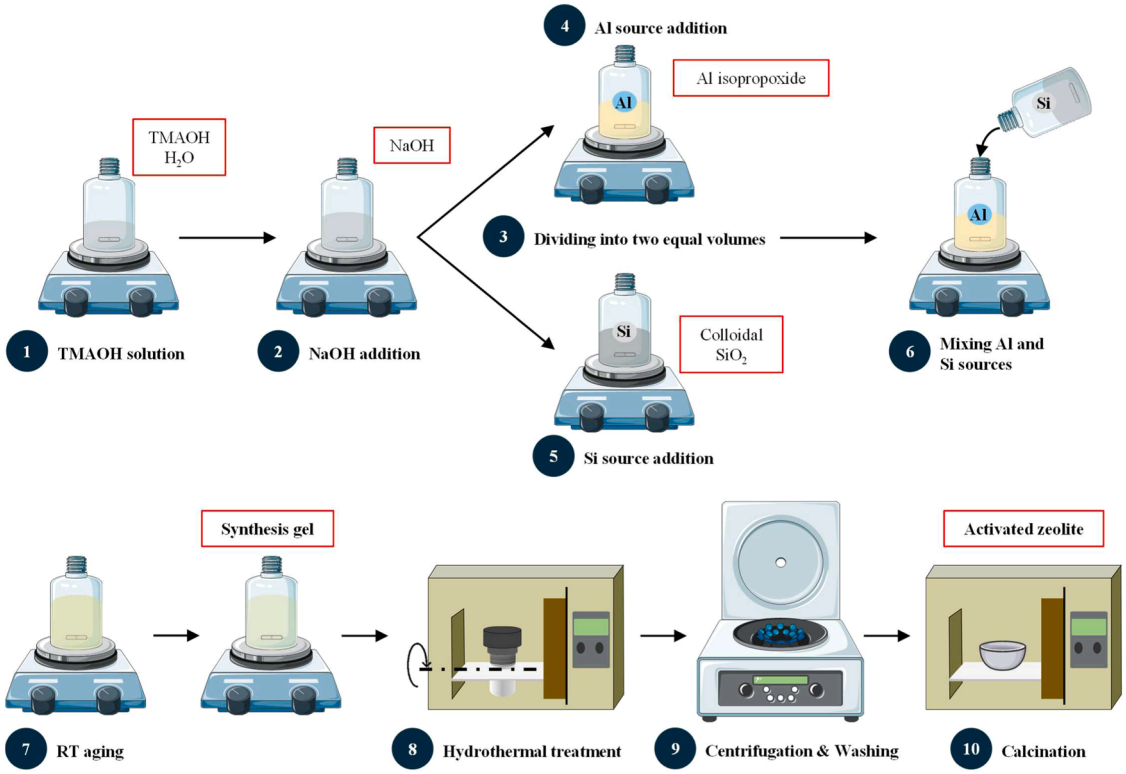

Fig. 1. Zeolite synthesis experimental procedure scheme (some images provided by Servier Medical Art (https://smart.servier.com), licensed under CC BY 4.0 (https://creativecommons.org/licenses/by/4.0/)).

images allowing more accurate particle size measurements. In this case, 100 size measurements were averaged.

2.3.3. Adsorption isotherms

Textural properties were assessed by N_2 and CO_2 physisorption isotherms. N_2 isotherms were recorded at -196 °C up to $p/p^\circ = 1$ in a Micromeritics TriStar 3000. Calcined zeolite powders were previously de-gassed following two steps in a Micromeritics VacPrep™: first at 100 °C for 1 h (10 °C·min^{-1}) and then at 200 °C for 10 h (1 °C·min^{-1}). From the N_2 physisorption data, the specific surface area (SSA) was calculated according to the Brunauer-Emmett-Teller (BET) and Langmuir methods, applied in the range of p/p° 0.07–0.2. Micropore volume was obtained employing the t-plot method in the thickness range of 0.34–0.5 nm. CO_2 isotherms were measured at 0 °C up to 100 kPa in a Micromeritics ASAP 2020. Calcined zeolites were previously de-gassed following two steps: first at 90 °C for 30 min (10 °C·min^{-1}) and then at 200 °C for 8 h (10 °C·min^{-1}) in the degas ASAP 2020 port. In addition, immediately prior analysis, samples were manually evacuated at 190 °C for 2–3 h. From the CO_2 adsorption data, the SSA and micropore volume were obtained according to the Dubinin-Radushkevich (DR) method, in the range of log $(p^\circ/p)^2$ 10–14. For both analyses, around 100 mg of sample were employed and the results were evaluated with MicroActive version 7.0 software.

2.3.4. Dynamic light scattering

Dynamic light scattering (DLS) was measured employing a Brookhaven BI-90 Plus Particle Size Analyzer. The hydrodynamic diameter was measured directly from zeolite synthesis slurries prior calcination, which were further diluted in H_2O and sonicated during 30 min.

2.3.5. Thermogravimetric analysis

Thermogravimetric analysis (TGA) was conducted in a Mettler Toledo TGA/STDA 851e. A small amount of zeolite powder was taken and placed in a 70 μL alumina crucible. In all experiments samples were heated from 35 °C to 700 °C (heating rate of 10 °C·min^{-1}) under a synthetic air atmosphere (15 cm^3 (STP)·min^{-1}).

2.3.6. Fourier transform infrared spectroscopy

Fourier transform infrared spectroscopy (FTIR) analysis weas carried out in a Bruker Vertex 70 spectrometer equipped with a DTGS detector and a Golden Gate diamond attenuated total reflectance (ATR). Zeolite spectra were recorded in the 4000–600 cm^{-1} wavenumber range at a resolution of 4 cm^{-1}.

3. Results and discussion

Although natural zeolites generally exhibit low Si/Al ratios, those with Si/Al atomic ratios close to 1 are synthetic as happens with zeolite A. Among the various synthesis protocols of zeolite A, the OSDA route is based on employing TMAOH. While OSDAs are typically used to produce more siliceous zeolites, in the case of zeolite A, TMAOH also promotes the nucleation stage, resulting in small particles with narrow distributions, without essentially affecting the Si/Al ratio of the zeolite. Zeolite A is generally obtained as a metastable phase that can be transformed into denser phases [33]. Therefore, the hydrothermal temperature for its synthesis is typically restricted to 100 °C or less, while the crystallization time does not tend to exceed 24 h under these conditions (**Table S1**). The preliminary experiments carried out here served to establish that, for a given composition, temperatures below 100 °C resulted in incomplete crystallization, while extending the synthesis from 12 h to 24 h yielded larger crystals (392 ± 63 nm vs. 482 ± 72 nm, **Figure S1**).

Table 1 summarizes the syntheses carried out, in which the different synthesis gels were aged at room temperature for 3 days and subsequently subjected to a hydrothermal process at 100 °C for 12 h. Briefly, the experiments listed in Table 1 evaluate the influence of the OSDA/Na^+ ratio at constant Si/Al atomic ratio (#1–10); and the effect of the Si/Al ratio in OSDA-free conditions (#9, #11–13) and at constant OSDA/

Table 1
Relevant synthesis gel compositions. In all syntheses, a hydrothermal treatment at 100 °C for 12 h was performed after 3 days of aging.

Entry	Parameter	Synthesis gel composition (mol)						
		SiO_2	Al_2O_3	H_2O	$(TMA)_2O$	Na_2O	TMA^+/Na^+	Si/Al
#1	TMA^+/Na^+	6.0	1.0	350.0	7.8	0.2	40	3
#2					7.8	0.3	30	
#3					7.6	0.4	20	
#4					7.3	0.7	10	
#5					6.7	1.3	5	
#6					6.2	1.8	3.5	
#7					5.4	2.7	2	
#8					2.7	5.3	0.5	
#9					0.0	8.0	0	
#10				190.0	7.8	0.2	40	
#9	Si/Al	6.0	1.0	350.0	0.0	8.0	0	3
#11		4.1						2
#12		2.0						1
#13		1.8						0.9
#14	Si/Al	9.9	1.0	350.0	7.8	0.2	40	5
#15		8.0						4
#1		6.0						3
#16		4.1						2
#17		2.0						1
#18		1.8						0.9
#19		1.5						0.75

Na^+ ratio (#1, #14–19). As shown, the OH^- molar ratio, to which both TMAOH and NaOH contribute, was fixed at 16; and the study was restricted to employing Na^+ as inorganic extraframework cation.

3.1. Zeolite phase determination

The PXRD patterns from Fig. 2 demonstrate a phase competition between different crystal polymorphs. From a structural point of view, there are some similarities between zeolite LTA and other zeolitic frameworks such as FAU, SOD and EMT [9,21], some of which appear as impurities in certain syntheses, as discussed below.

Given the obvious economic and environmental considerations, it would be preferable to avoid the use of OSDAs. Nevertheless, as evidenced by Maldonado et al. [33], different Na-zeolite polymorphs can crystallize at OSDA-free conditions. Fig. 2a shows that only at a Si/Al atomic ratio of 1 pure LTA zeolite crystals were obtained, while higher ratios promoted the crystallization of the more Si-rich FAU-type framework. Interestingly, at Si/Al<1, SOD-type zeolite impurities coexist with the LTA phase. As a result of the Si/Al ratios used in this work, the obtained LTA zeolites are zeolite A, while the FAU-type zeolites are zeolite X (typically zeolite Y corresponds to higher Si/Al ratios [35]).

Introducing TMA^+ as OSDA extends the range of Si/Al ratios over which the LTA framework can be obtained (Fig. 2b). In this case, FAU impurities appear together with the LTA phase only at Si/Al atomic ratios of 4 and higher. At the boundary of the LTA region (Si/Al atomic ratio of 3), pure LTA phases were obtained at OSDA/Na^+ ratios as low as 2 (Fig. 2c), while lower ratios resulted in pure FAU phases.

The PXRD patterns of Fig. 2 correspond to zeolite syntheses conducted at fixed OH^-/H_2O in the initial gel. Therefore, it is possible to

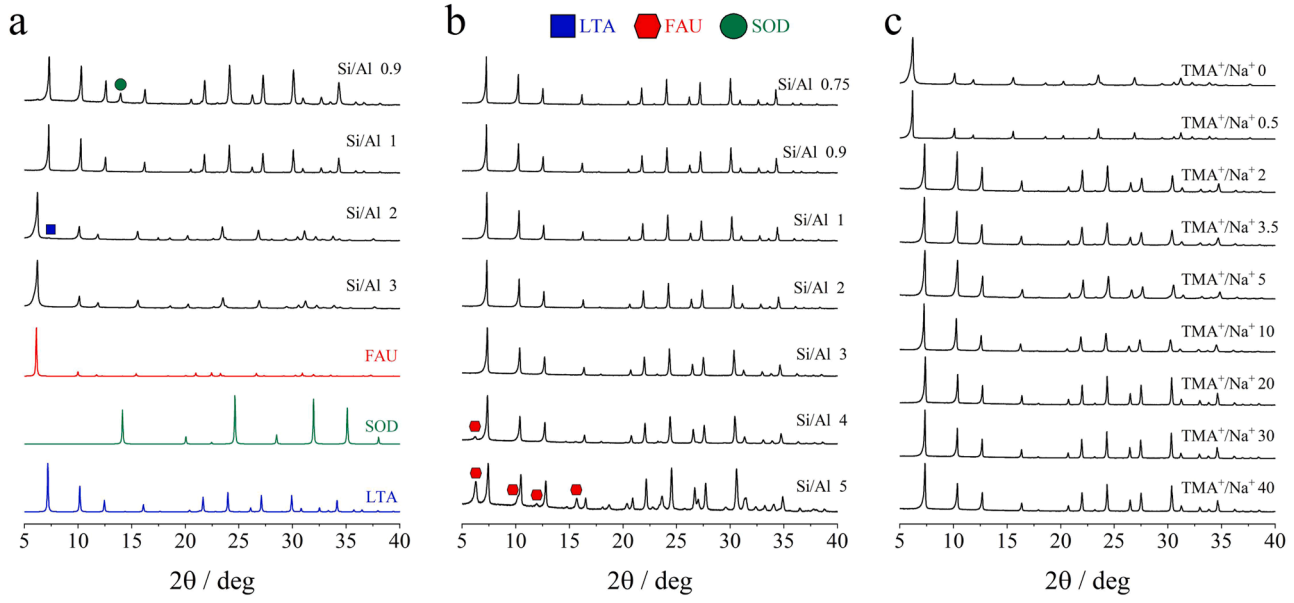

Fig. 2. Normalized PXRD patterns of OSDA-free syntheses alongside with the simulated patterns for FAU (red), SOD (green) and LTA (blue) frameworks (a, corresponds to entries #9, #11–13 from Table 1), syntheses varying the Si/Al molar ratio at constant OSDA/ Na^+ molar ratio (b, corresponds to entries #1, #14–19 from Table 1), and syntheses varying the OSDA to Na^+ molar ratio at constant Si/Al molar ratio (c, corresponds to entries #1–9 from Table 1). CIF files obtained from the Database of Zeolite Structures [14] and simulated PXRD with Mercury version 3.0 [34].

construct ternary diagrams restricting the composition to sodium, aluminum and silicon, and normalizing the values. The missing component, TMA_2O, can be determined by accounting for its contribution to the total OH^- molar composition. Fig. 3 shows the different phases obtained under various molar compositions. As illustrated, there is a specific region where pure LTA crystals are formed according to PXRD, while different polymorphs or impurities appear at the boundaries. This agrees with the fact that, as explained before, zeolite crystallization is a complex process and different zeolite phases that share similar structural features can crystallize in slightly different synthesis conditions. In the case of the LTA, FAU and SOD type structures, they can crystallize as low silica zeolites (Si/Al ≤2) and have in common the *sod* (or so-called *β-cage*) composite building unit. Therefore, it is important to identify that composition region in which a specific zeolite phase formation is favored.

3.2. Particle size and morphology

Zeolite syntheses were further analyzed by SEM to obtain detailed information regarding the particle size and morphology. In some cases, it was possible to detect the presence of minor impurities, not detectable by PXRD, by their distinct morphology [33], given that LTA, FAU and SOD zeolite phases exhibit different crystal habits. LTA crystals tend to be cubic; FAU crystals can consist of aggregates with various shapes, such as octahedra [36]; and SOD crystals are generally rounded and can develop disk-like geometries [37].

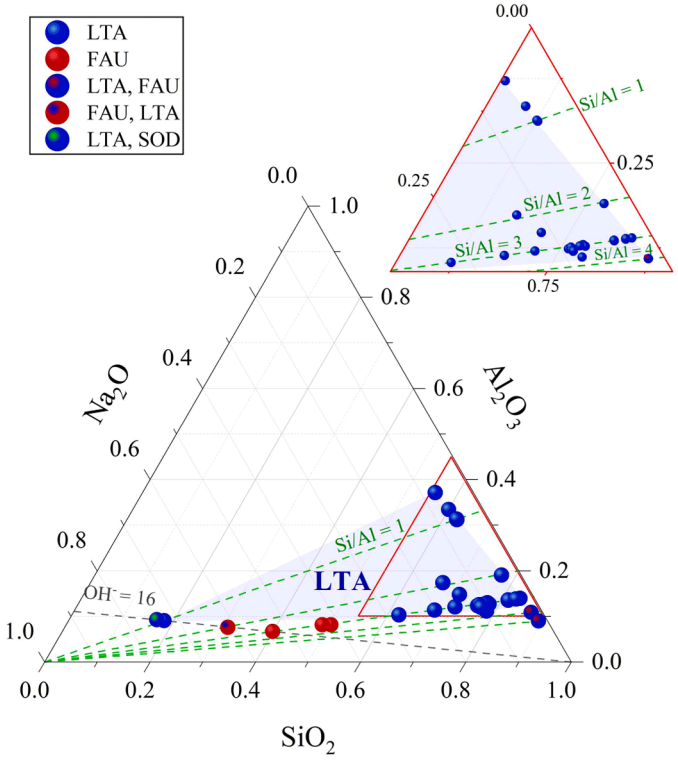

Fig. 3. Normalized ternary phase diagram of zeolites prepared at constant OH^- and H_2O molar compositions (16 and 350 respectively) in OSDA and OSDA-free conditions after hydrothermal treatment at 100 °C for 12 h. The shaded region corresponds to the formation of pure LTA phase. Each data point represents a zeolite synthesis in which pure LTA (blue), LTA containing FAU or SOD impurities (blue circle containing a red or green dot respectively), pure FAU (red) or FAU containing LTA impurities (red circle containing a blue dot) phases were identified according to their PXRD pattern. The grey dashed line indicates the molar composition at which $OH^- = 16$ is maintained in OSDA-free conditions, while green dashed lines indicate the Si/Al molar ratios of 1, 2, 3, 4 and 5 (from top to bottom respectively). The red triangle is enlarged at the top right.

3.2.1. Influence of the OSDA/Na^+ ratio

Fig. 4 shows the influence of employing different OSDA/Na^+ ratios from 40 to 0, which were examined at the Si/Al atomic ratio of 3. Previous studies demonstrated that for zeolite LTA, higher ratios of TMAOH resulted in lower particle sizes [24,25].

Interestingly, for the pure LTA phases obtained, an increase in the amount of OSDA did not consistently lower the particle size. The reduction in particle size was only observed for OSDA/Na^+ ratios of 40–20 (from particle sizes of ca. 149 ± 48 nm to 620 ± 178 nm). At an OSDA/Na^+ ratio of 10, the particle size distribution (PSD) was unexpectedly narrower and reduced (ca. 437 ± 54 nm) before continuing to increase (Fig. 4j). The synthesis at this ratio was carried out twice to confirm the smaller particle size (**Figure S2**). Additionally, to investigate the role of Na^+ independently, an experiment was conducted at the same OSDA/Na^+ ratio (10) but using a higher TMA_2O molar composition (TMA_2O = 7.8, analogous to entry #1 from Table 1, which yielded a particle size of 149 ± 48 nm). For this purpose, NaCl was added to the synthesis gel to maintain the fixed OH^- molar composition. Although it has been reported that the presence of Cl^- ions can direct the formation of the FAU phase (in OSDA free conditions) [35,38], in this case pure LTA-type zeolites were only obtained. The resulting particle size and morphology were analogous to those obtained from the previous synthesis at an OSDA/Na^+ = 10 (**Figure S3**). This suggests that the OSDA/Na^+ ratio is more critical in determining the particle size than the total amount of OSDA, and that the synthesis of nanosized zeolite NaA results from high OSDA/Na^+ ratios rather than high OSDA concentrations. However, as it will be discussed below, such high OSDA/Na^+ ratios inevitably give low yields. Moreover, for certain syntheses, the influence of employing a tumbling system during the hydrothermal treatment was also evaluated, seeking to enhance the nutrient mixture and produce a more homogeneous and smaller PSD. The experiments corresponding to entries #2–4 were repeated under these conditions and as shown in **Figure S4**, the tumbling system did not provide smaller or narrower particle sizes.

The SEM images of Fig. 4 show that, in addition to this counterintuitive result about crystal size, a clear change in morphology occurred at an OSDA/Na^+ ratio of 10 (Fig. 4d). Syntheses at higher ratios resulted in rounded cubes (Fig. 4a–c), whereas at lower ratios, zeolite particles exhibited cubes with sharp edges, and some impurities, likely SOD and FAU phases, began to appear (Fig. 4d–g and **Figure S5**).

It has been shown that in the presence of TMA^+ and Na^+, sodium cations, which are high charge-density cations, facilitate the formation of *d4r* units, while TMA^+ (low charge-density OSDA) participates in the formation of *sod* cages [39], both units necessary for zeolite LTA crystallization. The observed results may be attributable to the interplay between sodium and TMA^+ ions. On the one hand, hydrated sodium cations act as templates around which TO_4 tetrahedra regroup, these cations being essential to counterbalance the negative charge introduced by framework aluminium, facilitating crystallization. On the other hand, due to their larger diameter and lower charge-density, TMA^+ ions are less effective than sodium at balancing the framework aluminium, despite serving as templates to promote nucleation. Therefore, they possibly hinder the subsequent crystal growth. Sodium-deficient synthesis gels (from TMA^+/Na^+ 20 onwards) lack one of the species required for zeolite NaA crystallization. At these conditions, the smooth-edged cubes could result from a lower crystallization rate. In this crystallization regime, a higher consumption of small crystals by the Ostwald ripening mechanism seeks to explain the reduction in the particle size at TMA^+/Na^+ = 10, in which the higher amount of sodium ions would enable a faster crystallization that reduces the coalescence of small crystals. Consequently, zeolite particles crystallize as sharp-edged cubes. On this basis, **Figure S6** illustrates the mechanistic scheme of this hypothesis.

Pure FAU phases demonstrate clearly distinct morphology. In this case, under OSDA-free conditions, smaller aggregates of regular particles were obtained (Fig. 4i), whereas a low OSDA/Na^+ ratio (0.5)

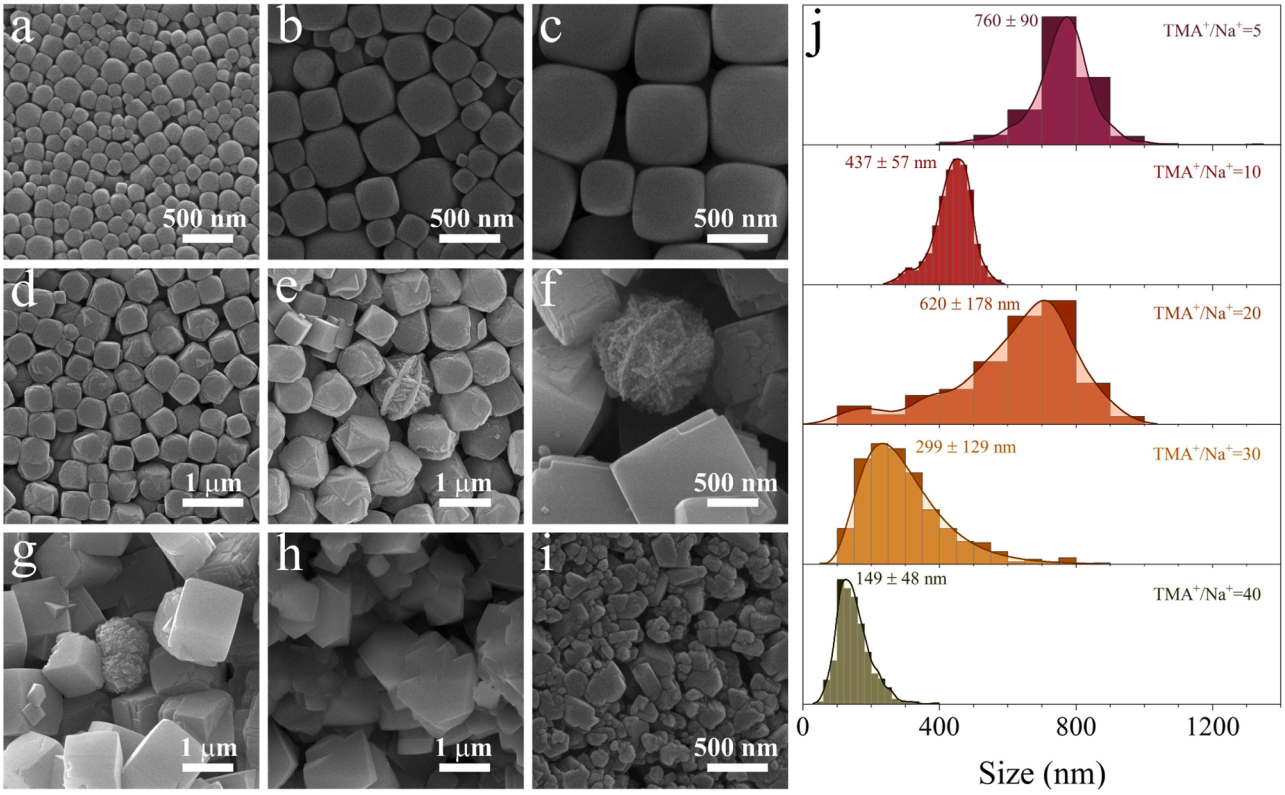

Fig. 4. SEM images of zeolite syntheses at OSDA/Na^+ molar ratios of 40, 30, 20, 10, 5, 3.5, 2, 0.5 and 0 (a-i correspond, respectively, to entries #1–9 from Table 1), and particle size distributions (PSD) for pure LTA cubic zeolites (OSDA/Na^+molar ratios of 40, 30, 20, 10 and 5) (j).

yielded aggregates of much larger particles (Fig. 4h).

3.2.2. *Influence of the Si/Al ratio in OSDA synthesis*

To test the influence of varying the Si/Al ratio on the particle size, some additional experiments were conducted at an OSDA/Na^+ ratio of 40. The results proved that FAU impurities began to appear exclusively in Si-rich solutions (Si/Al 4–5) in accordance with PXRD. SEM images of these syntheses revealed two distinct morphologies (Fig. 5a and b): rounded cubes, likely those corresponding to the LTA phase, and smaller aggregates, identified as the FAU phase. At intermediate Si/Al atomic ratios (Si/Al 1–3), the syntheses yielded rounded cubic LTA particles (Fig. 4a and Fig. 5c and d), with the smallest particle sizes observed in the more Si-rich environments (**Figure S7**). Al-rich solutions (Si/Al 0.75–0.9) resulted in the formation of pure LTA particles along with some undefined aluminosilicate particles (Fig. 5e and f), which were enriched in aluminum as confirmed by EDX (**Figure S8**). According to the Löwenstein's rule, no Al-O-Al linkages can occur [15], therefore, zeolite crystals with lower Si/Al atomic ratios than 1 are not possible.

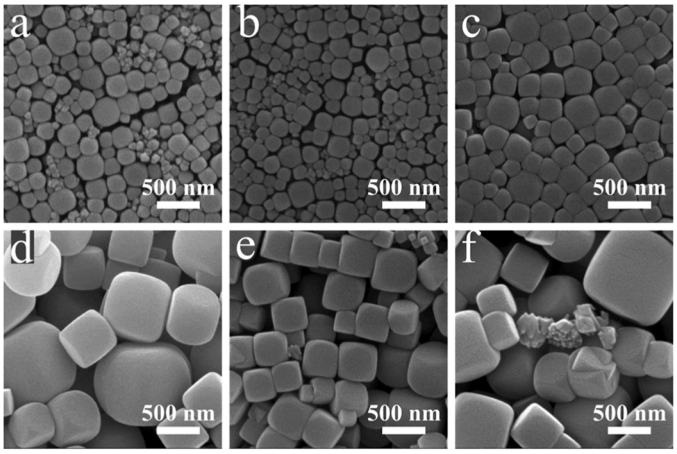

Fig. 5. SEM images of zeolite OSDA-based syntheses at Si/Al molar ratios of 5, 4, 2, 1, 0.9 and 0.75 (a-f correspond, respectively, to entries #14–19 from Table 1).

It has been widely reported that ageing prior crystallization can be employed to control the crystal size of zeolites by favoring the nucleation step [21,40]. For instance, Alfaro et al. [41], found that the aging time was crucial for reducing the particle size of zeolite LTA while conducting the synthesis in the absence of OSDAs. To investigate this, the synthesis gel with a Si/Al atomic ratio of 1, which had previously shown large particle sizes (Fig. 5d and **Figure S7**a), was subjected to 12 days of aging (three times longer than usual) at room temperature. However, neither a decrease in particle size nor a narrower PSD was observed (**Figure S9**). These results are aligned with previous studies employing TMAOH as OSDA, in which no further particle size reduction after 3 days of nucleation occurred [24,25]. Specifically, Mintova et al. [27], demonstrated that the "birth" of crystalline zeolite A at room temperature is triggered within the first 3 days.

3.2.3. *OSDA-free synthesis*

PXRD analysis (Fig. 2) revealed that at OSDA-free conditions, pure LTA crystals were exclusively obtained at a Si/Al atomic ratio of 1. In more Si-rich solutions, the LTA phase emerged as a minor component alongside the dominant FAU crystals, while at lower Si/Al ratios, both SOD and LTA phases were observed. SEM images of such syntheses show that FAU phases consist of aggregates of irregular faceted particles (Fig. 6a and b).

In the case of the pure LTA crystals, cubes with chamfered edges with certain crystal intergrowth (twin crystals) were identified (Fig. 6c and d), in contrast with the rounded and smaller cubes (393 ± 160 nm vs. 623 ± 103 nm, **Figure S10**) that grew in the analogous synthesis at high

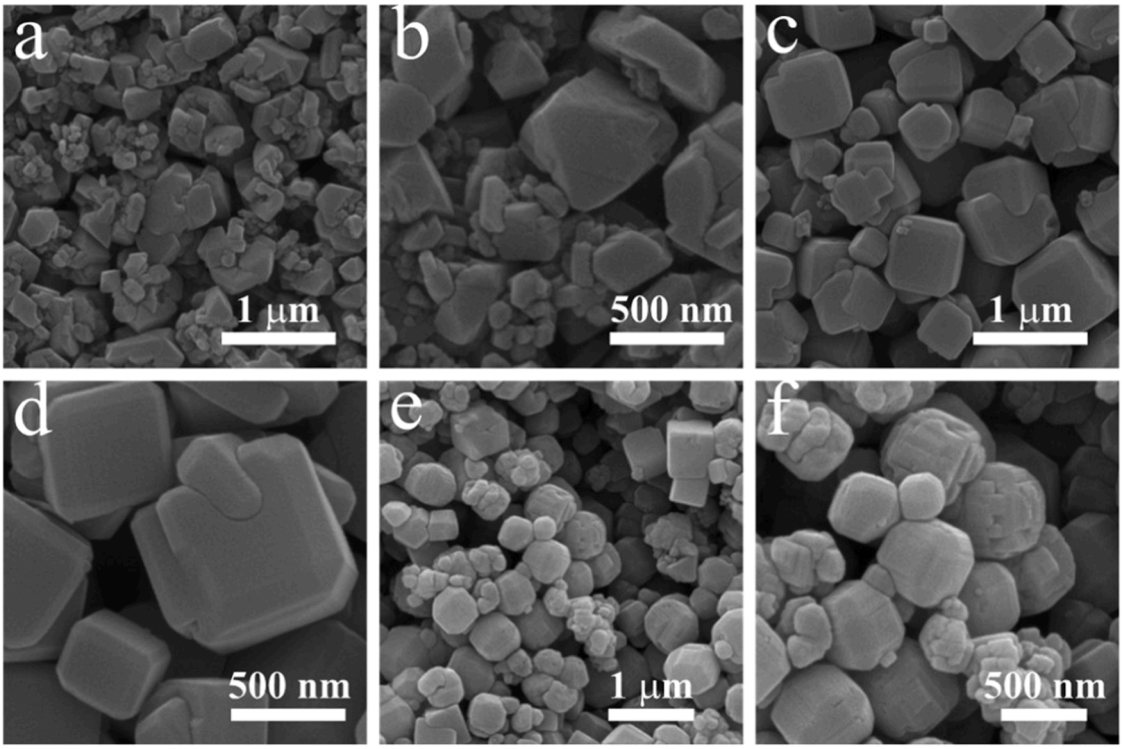

Fig. 6. SEM images of the different zeolite particle morphologies from the OSDA-free syntheses at Si/Al molar ratios of 2 (a and b), 1 (c and d), and 0.9 (e,f) corresponding, respectively, to entries #11–13 from Table 1.

OSDA/Na^+ ratio (Fig. 5c and d). However, the SOD crystals appeared as more spherical particles mixed with cubic LTA particles (Fig. 6e and f).

3.2.4. *Increasing supersaturation*

The influence of the water content has been evaluated by reducing it by nearly one-half at high OSDA/Na^+ conditions (Table 1 #10). Increasing the nutrient concentration by reducing the water content in zeolite synthesis gels leads to an increase in the concentration of all species (SiO_2, Al_2O_3, TMA_2O and Na_2O), and thus an increase in supersaturation, which favors nucleation [20]. Nevertheless, it does not necessarily increase the solution pH [33]. For example, the calculated pH values for entry #10 and its high-water content analog, entry #1, are 14.7 and 14.4, respectively. In this case, a synthesis at lower water content yielded pure LTA crystals (**Figure S11**), with the particle size reduced by nearly 40 % (149 ± 48 nm vs. 90 ± 27 nm, Fig. 7a), without detecting any zeolite morphology other than the LTA one. This synthesis was replicated two more times, and the results were consistent (85 ± 23 nm and 80 ± 23 nm, **Figure S12**), indicating that for the OSDA-based synthesis of zeolite A, the nutrient concentration is of major importance regarding the size of the resulting particles. For these small crystals, TEM provided higher-resolution images (Fig. 7b), allowing more accurate particle size measurements (68 ± 25 nm). Such particle size is among the smallest reported in the literature for zeolite A (**Table S1**).

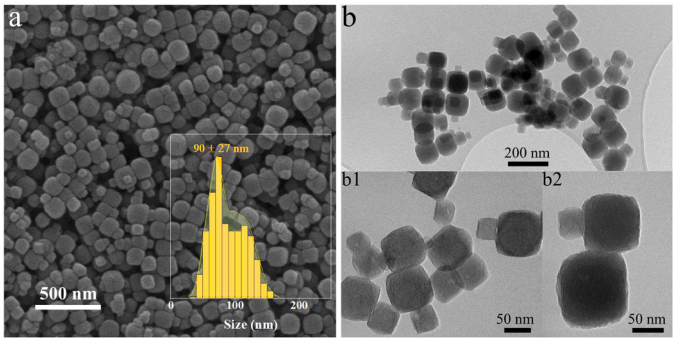

Fig. 7. SEM and TEM images of the low-water zeolite synthesis (entry #10 of Table 1) (a and b respectively). The inset in (a) shows the PSD, and lattice fringes are visible in (b1).

3.3. *Zeolite synthesis characterization*

Table 2 presents more detailed results regarding SEM, EDX, PXRD, DLS and the obtained yields of each synthesis. For the sake of clarity, these results have been illustrated in **Figures S13–15**.

The Si/Al ratio of the framework determines some important features of the resulting zeolite. Although zeolite A ideally has a Si/Al atomic ratio of 1, the aluminum content in the LTA framework can vary. For instance, Corma et al. [42], prepared the pure-silica analogue of zeolite A (ITQ-29) by means of supramolecular self-assembly of two cationic OSDAs. However, the hydrothermal synthesis of zeolite A employing TMAOH typically yields a narrow Si/Al range of 1 to 2 (**Table S1**). Importantly, as mentioned earlier, the incorporation of each aluminum atom into the zeolite framework entails a negative charge that must be compensated by the extraframework cations, in this case Na^+. Therefore, in the OSDA-based syntheses at a fixed Si/Al atomic ratio (Si/Al = 3), a higher OSDA/Na^+ ratio would be expected to result in a lower aluminum content. Nevertheless, this trend appears to be disrupted at the OSDA/Na^+ ratio of 10, where both particle size and morphology are altered. At lower OSDA/Na^+ ratios, the estimated Si/Al ratios by EDX range from 1.70 to 2.32. In any case, the estimated Si/Al atomic ratio by EDX (1.59–2.32) is lower than that of the synthesis gel (3) (**Figure S13**a).

At OSDA-free conditions (**Figure S13**b), higher Si/Al synthesis ratios (which yielded FAU phases) resulted in a lower aluminum content, while more aluminum is incorporated for the pure LTA framework, which was prepared in Al-rich conditions. In this case, the estimated Si/Al atomic ratio was lower than that of the synthesis gel until the starting formulation was reduced to Si/Al = 1, below which apparently it was

Table 2
Summary of the SEM, PXRD and DLS results for relevant zeolite syntheses.

Entry	SEM		PXRD			DLS		Yield[d]
	Size ± (nm)	Si/Al[a]	Crystal phase (CI)[b]	a (Å)[c]	Crystallite size (nm)[c]	Eff. Diam. (nm)	PDI	
#1	149 ± 48	1.69 ± 0.10	LTA (70 %)	24.08	31	239	0.041	15 %
#2	299 ± 129	1.64 ± 0.11	LTA (70 %)	24.09	38	386	0.131	21 %
#3	620 ± 178	1.59 ± 0.14	LTA (72 %)	24.01	35	815	0.069	24 %
#4	437 ± 54	1.68 ± 0.05	LTA (100 %)	24.32	33	596	0.030	48 %
#5	760 ± 90	2.32 ± 0.23	LTA (94 %)	24.06	30	1285	0.215	60 %
#6	-	1.76 ± 0.08	LTA (82 %)	24.20	29	-	-	60 %
#7	-	2.09 ± 0.15	LTA (81 %)	24.14	33	-	-	60 %
#8	-	1.77 ± 0.05	FAU (100 %)	24.70	35	-	-	48 %
#9	-	1.70 ± 0.06	FAU (74 %)	24.68	20	-	-	38 %
#10	90 ± 27[e]	1.59 ± 0	LTA (74 %)	24.21	24	-	-	17 %
#9	-	1.70 ± 0.06	FAU (74 %)	24.68	20	-	-	38 %
#11	-	1.41 ± 0	FAU, LTA	-	-	-	-	37 %
#12	626 ± 103	1.17 ± 0.05	LTA (77 %)	24.32	37	1126	0.210	34 %
#13	-	1.20 ± 0.05	LTA, SOD	-	-	-	-	36 %
#14	-	2.13 ± 0.13	LTA, FAU	-	-	-	-	12 %
#15	-	1.98 ± 0.10	LTA, FAU	-	-	-	-	12 %
#1	149 ± 48	1.69 ± 0.10	LTA (70 %)	24.08	31	239	0.041	15 %
#16	231 ± 68	1.58 ± 0.01	LTA (76 %)	24.21	37	324	0.040	16 %
#17	393 ± 160	1.29 ± 0.01	LTA (76 %)	24.29	42	824	0.135	20 %
#18	-	1.19 ± 0.04	LTA (72 %)	24.34	37	-	-	19 %
#19	-	1.14 ± 0.02	LTA (69 %)	24.38	39	-	-	13 %

[a] Atomic ratio determined from EDX analysis.
[b] Crystallinity of LTA and FAU phases relative to syntheses #4 and #8, respectively, calculated from the sum of peak areas: (200), (220) and (222) planes for LTA phase, and (111), (220), and (311) planes for FAU.
[c] Considering (200), (220) and (222) planes for pure LTA phases and (111), (220) and (311) planes for pure FAU phases.
[d] Yield was calculated as the ratio between the mass of calcined zeolite and the total mass of SiO_2, Al_2O_3 and Na_2O.
[e] The size measured by TEM is 68 ± 25 nm

not possible to incorporate more aluminum and the measured Si/Al ratios exceed the former gel composition. A similar trend was observed for syntheses conducted at fixed OSDA/Na^+ ratio while varying the Si/Al (**Figure S13**c): the aluminum content increased systematically with decreasing synthesis gel Si/Al, until the threshold of Si/Al = 1 was reached, beyond which the measured Si/Al ratios exceed that of the synthesis gel.

Regarding Si/Al ratio determination, selected zeolite samples were analyzed by ICP-OES (Table S2). Although slight variations were observed, the values obtained by ICP-OES are in a similar range to those obtained by EDX.

Apart from qualitative phase identification, PXRD data allowed to determine the lattice parameter and crystallite size of the obtained zeolites. For pure LTA frameworks, the obtained lattice parameter is ~24.2 Å, whilst for pure FAU phases it expands to ~24.7 Å. Consistent with the registered values at the IZA for the NaA (LTA) and NaX (FAU) phases, 24.6 Å and 25.1 Å, respectively [43]. Generally, for a given zeolite phase it is expected that with increasing framework aluminum the lattice parameter increases [44]. Such linear relationship was observed for the syntheses varying the Si/Al composition (**Figure S14**). From the calculated crystallite sizes by the Scherrer equation, no correlation was found between particle and crystallite sizes (Table 2), suggesting the presence of polycrystalline nanoparticles [45], which may affect their intrinsic diffusion as showed for other zeolites [46]. Finally, the relative crystallinity of LTA or FAU phases was obtained by considering the peak areas of the first three reflections. Interestingly, it suggests that the crystallization of zeolite A is favored when employing an OSDA/Na^+ ratio of 10, in which sodium and aluminum are in almost the same molar composition ($1Al_2O_3$: $0.7Na_2O$), and for Si/Al atomic ratios between 1–2 (**Figure S15**).

Although DLS measurements were taken from the diluted as-synthetized zeolite NaA slurries to limit particle aggregation, a positive deviation with SEM results was obtained (Table 2 and **Figure S16**). DLS hydrodynamic diameter measurements were obtained directly from the scattering intensity signal. Given that these results are weighed by the different size fractions within each size distribution ($I_{scattering} \propto d^6$) [47], the observed size distribution may be overestimated due to the presence of larger particles (within each size distribution) or aggregates. Moreover, in comparison with the SEM PSD, larger deviations were observed for those zeolites with a higher aluminum content, consistent with a thicker solvation sphere due to higher hydrophilicity. Nevertheless, DLS values followed the same size trends observed in SEM.

FTIR (**Figure S17–19**) and TGA (**Figure S20–22**) analyses (see Supporting Information) reveal no significant variations among the samples. Finally, although the synthesis gel compositions did not follow the expected stoichiometry of zeolite NaA ($[Na_{12}(H_2O)_{27}]_8[Al_{12}Si_{12}O_{48}]_8$)[43], the synthesis yields were calculated as the ratio between the mass of calcined zeolite and the total mass of SiO_2, Al_2O_3 and Na_2O in the parent gel. Regarding the preparations carried out by varying the OSDA/Na^+ composition, at high ratios of this parameter (TMA^+/Na^+ = 10–40), all the syntheses are sodium-deficient; consequently, the zeolite formation is restricted and the obtained yields are low (15–48 %). The incorporation of sodium cations leads to an increase in the calculated yield (60 %) until the synthesis gels become increasingly aluminum-deficient. Finally, the zeolite yield decreases in the region where FAU crystallization is favored (17–48 %) (**Figure S23**a). In those syntheses in absence of OSDA, sodium is in large excess, and the different Si/Al ratios gave similar yields for the crystalized LTA and FAU phases (~36 %), the latter being obtained in the more Si-rich compositions (**Figure S23**b).

Considering that the syntheses varying the Si/Al ratio were prepared with the highest OSDA/Na^+ ratio tested (40), they resulted in low yields due to the sodium deficiency (12–20 %). The yield increased slightly for the synthesis at Si/Al = 1 (20 %), consistent with the ideal zeolite A stoichiometry (**Figure S23**c). Although it has been described the role of sodium cations as SDA towards zeolite crystallization [21], the incorporation of an OSDA as TMA^+, which represents the smallest quaternary alkylammonium cation, is expected to selectively direct the formation of zeolite A. Therefore, the higher LTA yields were achieved for syntheses conducted employing TMA^+ as OSDA, in sodium-rich environments. However, to obtain nanosized zeolites with reduced particle size it is required to employ sodium-deficient synthesis and high OSDA/Na^+

ratios. This substantial use of OSDA inevitably raises production costs and necessitates the treatment of toxic residues to mitigate potential environmental impacts.

3.4. Textural properties

Adsorption measurements provide information regarding the porosity of zeolites. Those with the LTA framework, such as zeolite A, are classified as small-pore zeolites given the size of the 8-membered ring of the LTA composite building unit (also called *α-cage*). Specifically, the Na^+ exchanged form of zeolite A is designated as zeolite 4A (also known as zeolite NaA), as its 8-ring openings are approximately 4 Å [43]. Fig. 8 shows the N_2 adsorption-desorption isotherms recorded at -196 °C for the OSDA-based synthesis (OSDA/Na^+ = 40) at varying Si/Al conditions (Fig. 8a), as well as for the syntheses carried out with different OSDA/Na^+ compositions at a fixed Si/Al ratio (3) (Fig. 8b).

3.4.1. Nitrogen adsorption

Low Si/Al atomic ratios (Si/Al 0.75, 0.9 and 1) resulted in minimal N_2 adsorption (Fig. 8a inset), as reported previously for zeolite 4A with low Si/Al ratio [48,49], from which the calculated SSAs and micropore volume are negligible (entries #17–19 of Table 3). Nitrogen uptake is only detectable at relative pressures close to 1, which is related to capillary condensation between nanoparticles. As expected, a higher aluminum content is related to a low N_2 adsorption. Its incorporation implies the introduction of negative charges that are balanced by sodium cations. These charged species barely interact with nitrogen, which is nonpolar and has low polarizability and quadrupolar moments (**Table S3**), hindering its diffusion through the framework. Moreover, the incorporation of a higher number of sodium cations reduces the accessible volume.

Conversely, at higher Si/Al ratio the isotherms feature a sudden increase at low pressure, given by micropore filling, and an abrupt increase at high pressure featuring a small hysteresis loop, that can be explained considering the capillary condensation in mesopores created between nanoparticles (Fig. 8a). These isotherms can be categorized as type I according to the IUPAC [50]. In this case, the SSAs and micropore volumes confirm the high surface area and microporosity of the material, exhibiting slightly higher values at the highest Si/Al ratio: 564 $m^2 \cdot g^{-1}$ (BET), 742 $m^2 \cdot g^{-1}$ (Langmuir), and 0.25 $cm^3 \cdot g^{-1}$ for Si/Al = 3; and 513 $m^2 \cdot g^{-1}$ (BET), 675 $m^2 \cdot g^{-1}$ (Langmuir) and 0.23 $m^2 \cdot g^{-1}$ for Si/Al = 2 (Table 3).

Given that the syntheses varying the OSDA/Na^+ compositions were performed at the highest Si/Al atomic ratio (Si/Al = 3), the isotherms feature the same type I shape exhibited by microporous materials (Fig. 8b). SSAs and micropore values are in the 496–629 $m^2 \cdot g^{-1}$ (BET), 654–827 $m^2 \cdot g^{-1}$ (Langmuir), and 0.23–0.28 $cm^3 \cdot g^{-1}$ ranges, respectively.

It should be noted that a hysteresis loop appears from $p/p^\circ > 0.9$ in most of the samples, which is related to capillary condensation between nanoparticles, as previously observed.

In all cases, the SSA calculated using the Langmuir equation is higher than that determined by the BET theory. The latter, which is based on multilayer adsorption, is reported for its convenience as a standard for comparison with different adsorbents; while the Langmuir SSA is also calculated because the obtained isotherms are clearly type I, which supports the assumptions of monolayer adsorption. Besides, the BET method can miscalculate the SSA of ultra-microporous zeolites since pore filling occurs at lower pressure than the standard BET pressure range [51], and for these materials, the consistency criteria proposed by Rouquerol et al. [50], were not fulfilled.

3.4.2. Carbon dioxide adsorption

In any case, it has been demonstrated the suitability of CO_2 adsorption at 0 °C for the characterization of small pore zeolites [48]. As shown in Fig. 9, all the CO_2 adsorption isotherms exhibit an increase in the uptake at low pressures due to micropore filling, and then, as the porous system becomes saturated, adsorption plateaus. In this case, the adsorption was carried out at a higher temperature than with N_2, which helps to overcome diffusional limitations in micropores. Moreover, CO_2 has larger polarizability and quadrupolar moment than N_2, and a smaller kinetic diameter (**Table S3**). Both factors explain the higher affinity of zeolite 4A for CO_2, where electrostatic interactions occur between the zeolite cations and CO_2 [18].

In contrast to N_2 adsorption at -196 °C, zeolites at low Si/Al atomic ratios (Si/Al 1, 0.9 and 0.75) give type I isotherms (Fig. 9a), from which now is possible to obtain values of SSA and micropore volume through the DR method (entries #17–19 of Table 3). It should be noted that if nitrogen adsorption is performed at 0 °C (**Figure S24**), it shows a slightly higher adsorption than at -196 °C but without showing a type I isotherm characteristic of microporous materials.

Nevertheless, the zeolites with higher Si/Al ratio, which already

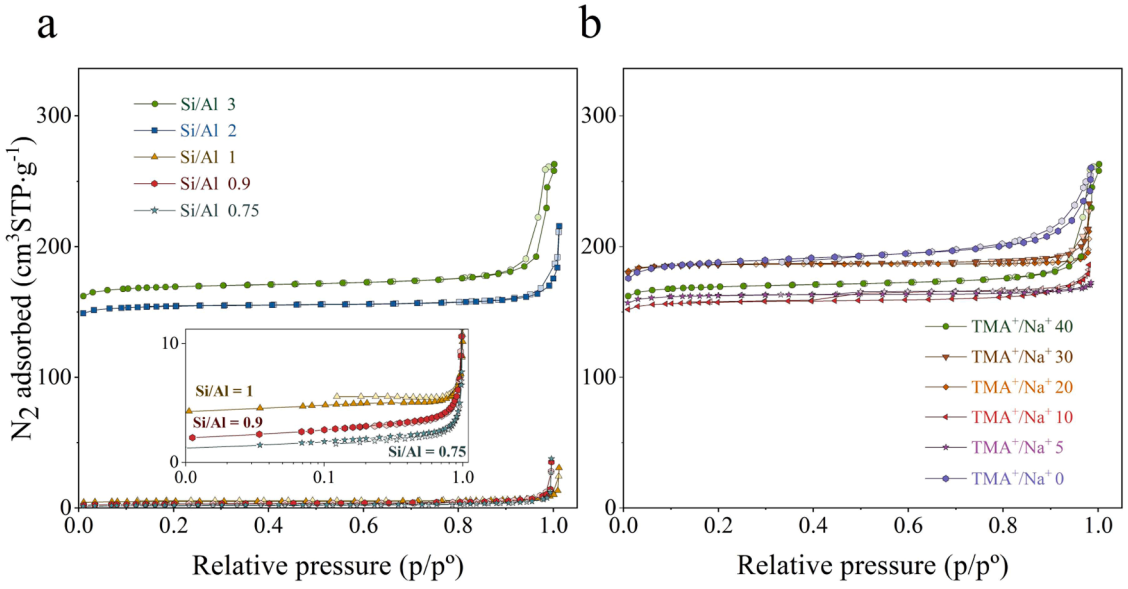

Fig. 8. N_2 adsorption-desorption isotherms at -196 °C of syntheses varying the Si/Al molar ratio at constant OSDA/Na^+ molar ratio (40) (a), and syntheses varying the OSDA/Na^+ molar ratio at constant Si/Al molar ratio (3) (b).

Table 3
Textural properties of relevant zeolite syntheses.

Entry	N_2 -196 °C			CO_2 0 °C		
	BET_{SSA} ($m^2 \cdot g^{-1}$)	V_{micro} ($cm^3 \cdot g^{-1}$)	$Langmuir_{SSA}$ ($m^2 \cdot g^{-1}$)	DR_{SSA} ($m^2 \cdot g^{-1}$)	V_{micro} ($cm^3 \cdot g^{-1}$)	Uptake ($mmol \cdot g^{-1}$) at 10/20 kPa
#1	564	0.25	742	857	0.34	4.6/4.9
#2	619	0.28	815	868	0.35	4.7/5.1
#3	618	0.28	813	861	0.35	4.7/5.1
#4	523	0.23	689	836	0.34	4.7/5.0
#5	540	0.24	710	786	0.31	4.4/4.8
#7	496	0.23	654	730	0.29	4.2/4.5
#9	629	0.27	827	1071	0.43	4.7/5.3
#10	452	0.18	595	758	0.30	4.2/4.5
#12	2	-	3	517	0.21	3.5/3.8
#1	564	0.25	742	857	0.34	4.6/4.9
#16	513	0.23	675	844	0.34	4.4/4.8
#17	17	-	22	695	0.28	3.9/4.3
#18	11	-	15	702	0.28	3.9/4.3
#19	7	-	10	583	0.23	3.7/4.1

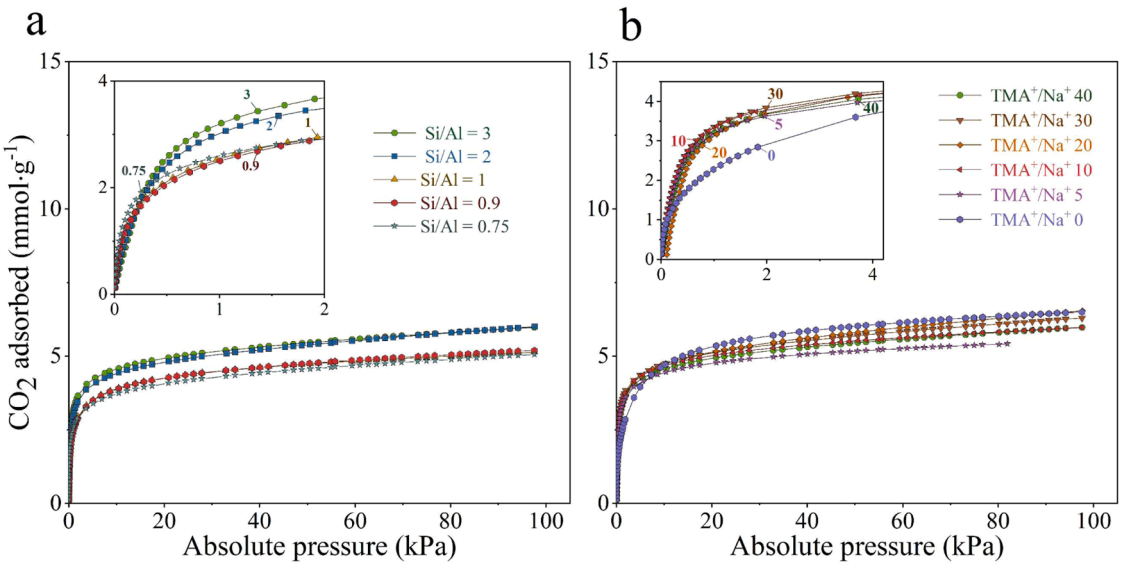

Fig. 9. CO_2 adsorption isotherms at 0 °C of syntheses varying the Si/Al molar ratio at constant OSDA/Na^+ molar ratio (40) (a), and syntheses varying the OSDA/Na^+ molar ratio at constant Si/Al molar ratio (3) (b).

exhibited N_2 adsorption, showed greater adsorption and, consequently, higher SSA (~850 $m^2 \cdot g^{-1}$) and micropore volume (0.34 $cm^3 \cdot g^{-1}$) values owing to the lower occupancy of the pore system by sodium cations.

No significant differences were observed among the LTA zeolites prepared with varying OSDA/Na^+compositions. SSA and micropore volumes averaged 823 $m^2 \cdot g^{-1}$ and 0.33 $cm^3 \cdot g^{-1}$ respectively (entries #1–5 and #7 of Table 3).

Interestingly, the OSDA-free synthesis that crystallized in the FAU framework yielded the highest SSA (1071 $m^2 \cdot g^{-1}$) and micropore volume (0.43 $cm^3 \cdot g^{-1}$) (entry #9 of Table 3). For this zeolite, micropore saturation occurs at slightly higher pressure, and the total adsorption capacity is greater than that of the LTA zeolites (Fig. 9). Owing to its larger pore diameter (12-ring aperture) and lower framework density (12.7 T/1000 $Å^3$ vs 12.9 T/1000 $Å^3$ for the FAU and LTA phases respectively [43]), zeolite 13X, commercial name for a representative low Si/Al FAU-type zeolite, has been reported to exhibit a greater CO_2 adsorption capacity compared to zeolite 4A [52–54]. Finally, it is worth mentioning that those samples with a combination of higher aluminum content and low N_2 adsorption (entries #12 and #17–19 of Table 3), show comparable CO_2 features (DR_{SSA}, V_{micro} and uptake) to the other samples, concluding that sodium cations in the zeolite do not impede the uptake of this molecule.

4. Conclusions

In a SiO_2-Al_2O_3-TMA_2O-Na_2O-H_2O system, there is a window of molar composition in which the crystallization of zeolite NaA is favored above other zeolite polymorphs. Nevertheless, the adjustment of the synthesis gel not only affects the crystal phase, but also the crystal size and morphology of the resulting zeolite particles.

The addition of TMAOH as OSDA directs the synthesis towards the crystallization of zeolite NaA, extending the range of synthesis gel Si/Al ratios from which zeolite NaA can be produced. Adding TMAOH at the expense of NaOH reduces the size of zeolite crystals, which are obtained as rounded cubes. Nevertheless, the relationship between size and the OSDA/Na^+ ratio is not linear: lowering the OSDA/Na^+ ratio increases the particle size up to a certain threshold (TMA^+/Na^+ = 10). At this threshold, particle morphology transitions to sharp-edged cubes which have a smaller particle size than certain syntheses carried out at a higher TMA^+/Na^+ ratio. The use of different gel Si/Al atomic ratios also affects the crystal size. From Si/Al = 1 to 3, crystal size decreases, and above Si/Al = 3, FAU impurities begin to appear. Increasing supersaturation by lowering the H_2O molar composition resulted in a reduction of the particle size. At Si/Al = 3 and TMA^+/Na^+ = 40, after 3 days of aging and 12 h at 100 °C for hydrothermal crystallization, zeolite particles down to 68 nm (as shown by TEM) were produced. Nevertheless, the smallest

particles were obtained in sodium-deficient systems, which results in a low total yield (per gram of nutrients).

The adsorption properties of the resulting zeolites are highly dependent on their chemical composition. Zeolites prepared with high gel Al compositions (Si/Al $\leq$ 1) show negligible N_2 adsorption, while zeolites prepared employing higher Si/Al ratios featured the type-I isotherm, given by microporous solids. Conversely, all the synthesized zeolites exhibited a type-I isotherm for CO_2 adsorption, demonstrating the higher affinity of zeolite NaA for CO_2.

In summary, we address a fraction of the different parameters involved in the OSDA-based hydrothermal synthesis of zeolite NaA, seeking to control the particle size. Nanosized zeolite particles will benefit from enhanced mass transfer through active surface sites and higher external surface areas for improved interaction with polymers. In consequence, leveraging the adsorption capability of zeolite NaA, these particles could be employed to efficiently fabricate mixed matrix membranes, paving the way for the development of thin-film nanocomposite membranes.

Funding sources

This work gratefully acknowledges grants PID2022-138582OB-I00 funded by MICIU/AEI/10.13039/501100011033/ and by "ERDF A way of making Europe". L. Güemes also thanks the Aragón Government (DGA) for his Ph.D. grant. Financial assistance from the Government of Aragón (T68_23R) is also acknowledged. CEX2023–001,286-S funded by MICIU/AEI/10.13039/501100011033/.

CRediT authorship contribution statement

Lucas Güemes: Writing – review & editing, Writing – original draft, Visualization, Validation, Methodology, Investigation, Formal analysis, Conceptualization. **Joaquín Coronas:** Writing – review & editing, Writing – original draft, Supervision, Resources, Project administration, Methodology, Funding acquisition, Conceptualization. **Carlos Téllez:** Writing – review & editing, Writing – original draft, Supervision, Resources, Project administration, Methodology, Funding acquisition, Conceptualization.

Declaration of competing interest

The authors declare that they have no known competing financial interests or personal relationships that could have appeared to influence the work reported in this paper

Acknowledgements

Authors would like to acknowledge the use of Servicio General de Apoyo a la Investigación-SAI, Universidad de Zaragoza, and the use of instrumentation as well as the technical advice provided by the National Facility ELECMI ICTS, node «Laboratorio de Microscopias Avanzadas (LMA)» at «Universidad de Zaragoza».

Supplementary materials

Supplementary material associated with this article can be found, in the online version, at doi:10.1016/j.surfin.2026.108989.

Data availability

Data will be made available on request.

References

[1] R. Gans, Alumino-silicate or artificial zeolite, US943535, 1909.
[2] J.M. Corkill, B.L. Madison, M.E. Burns, Detergent compositions containing sodium aluminosilicate builders, US4605509, 1986.
[3] R.C. Speak, P.H. McConnell, Fabric laundry compositions, US3154494, 1964.
[4] E. Pérez-Botella, S. Valencia, F. Rey, Zeolites in adsorption processes: state of the art and future prospects, Chem. Rev. 122 (2022) 17647–17695. https://doi.org/10.1021/acs.chemrev.2c00140.
[5] J.W. McBain, The Sorption of Gases and Vapours by Solids, G. Routledge, London, 1932.
[6] C. Martínez, A. Corma, Inorganic molecular sieves: preparation, modification and industrial application in catalytic processes, Coord. Chem. Rev. 255 (2011) 1558–1580, https://doi.org/10.1016/j.ccr.2011.03.014.
[7] A.F. Cronstedt, Rön och beskrifning om en obekant bärg art, som kallas Zeolites, Kongl Vetensk. Acad. Handl. Stockh. 17 (1756) 120. https://books.google.es/books?id=MSv-MQAACAAJ.
[8] H. Sainte-Claire Deville, Reproduction de la levyne, C. R. 54 (1862) 324–327.
[9] S.M. Auerbach, K.A. Carrado, P.K. Dutta, Handbook of Zeolite Science and Technology, CRC Press, 2003, https://doi.org/10.1201/9780203911167.
[10] W. Yan, Y. Li, F.-S. Xiao, Z. Liu, J. Yu, The future of zeolites, Chem. Mater. 36 (2024) 7103–7105, https://doi.org/10.1021/acs.chemmater.4c01675.
[11] R.M. Milton, Molecular sieve science and Technology, in: M.L. Occelli, H.E. Robson (Eds.), Zeolite Synthesis, American Chemical Society, 1989, pp. 1–10, https://doi.org/10.1021/bk-1989-0398.ch001.
[12] R.M. Barrer, P.J. Denny, Hydrothermal chemistry of the silicates. Part IX. Nitrogenous aluminosilicates, J. Chem. Soc. (Resumed) (1961) 971, https://doi.org/10.1039/jr9610000971.
[13] S.T. Wilson, B.M. Lok, C.A. Messina, T.R. Cannan, E.M. Flanigen, Aluminophosphate molecular sieves: a new class of microporous crystalline inorganic solids, J. Am. Chem. Soc. 104 (1982) 1146–1147, https://doi.org/10.1021/ja00368a062.
[14] C. Baerlocher, D. Brouwer, B. Marler, L.B. McCusker, Database of Zeolite structures, (2017). https://www.iza-structure.org/databases/(accessed October 9, 2025).
[15] W. Loewenstein, The distribution of aluminum in the tetrahedra of silicates and aluminates, Am. Mineral. 39 (1954) 92–96.
[16] M.J. Schwuger, M. Liphard, Fundamentals of phosphate substitution in detergents by zeolites, in: H.G. Karge, J. Weitkamp (Eds.), Zeolites As Catalysts, Sorbents and Detergent Builders, Elsevier, Amsterdam, 1989, pp. 673–690, https://doi.org/10.1016/S0167-2991(08)61021-6.
[17] F. Collins, A. Rozhkovskaya, J.G. Outram, G.J. Millar, A critical review of waste resources, synthesis, and applications for Zeolite LTA, Microporous Mesoporous Mater. 291 (2020) 109667, https://doi.org/10.1016/j.micromeso.2019.109667.
[18] D.G. Boer, J. Langerak, P.P. Pescarmona, Zeolites as selective adsorbents for CO_2 separation, ACS Appl. Energy Mater. 6 (2023) 2634–2656, https://doi.org/10.1021/acsaem.2c03605.
[19] F. Di Renzo, Zeolites as tailor-made catalysts: control of the crystal size, Catal. Today 41 (1998) 37–40, https://doi.org/10.1016/S0920-5861(98)00036-4.
[20] J. Yu, Synthesis of Zeolites, in: J. Čejka, H. van Bekkum, A. Corma, F. Schüth (Eds.), Introduction to Zeolite Science and Practice, 3rd ed., Elsevier B.V., Amsterdam, 2007, pp. 39–103, https://doi.org/10.1016/S0167-2991(07)80791-9.
[21] K. Byrappa, M. Yoshimura, Hydrothermal technology—Principles and applications, in: K. Byrappa, M. Yoshimura (Eds.), Handbook of Hydrothermal Technology, Elsevier, 2001, https://doi.org/10.1016/B978-081551445-9.50002-7.
[22] A. Jawor, B.-H. Jeong, E.M.V. Hoek, Synthesis, characterization, and ion-exchange properties of colloidal zeolite nanocrystals, J. Nanoparticle Res. 11 (2009) 1795–1803, https://doi.org/10.1007/s11051-009-9688-9.
[23] E. Biemmi, T. Bein, Assembly of nanozeolite monolayers on the gold substrates of piezoelectric sensors, Langmuir 24 (2008) 11196–11202, https://doi.org/10.1021/la8009892.
[24] S. Yu, S. Kwon, K. Na, Synthesis of LTA zeolites with controlled crystal sizes by variation of synthetic parameters: effect of Na^+ concentration, aging time, and hydrothermal conditions, J. Sol-Gel Sci. Technol. 98 (2021) 411–421, https://doi.org/10.1007/s10971-018-4850-4.
[25] M. Jafari, A. Nouri, M. Kazemimoghadam, T. Mohammadi, Investigations on hydrothermal synthesis parameters in preparation of nanoparticles of LTA zeolite with the aid of TMAOH, Powder. Technol. 237 (2013) 442–449, https://doi.org/10.1016/j.powtec.2012.12.031.
[26] G. Yang, X. Zhang, S. Liu, K.L. Yeung, J. Wang, A novel method for the assembly of nano-zeolite crystals on porous stainless steel microchannel and then zeolite film growth, J. Phys. Chem. Solids 68 (2007) 26–31, https://doi.org/10.1016/j.jpcs.2006.09.009.
[27] S. Mintova, N.H. Olson, V. Valtchev, T. Bein, Mechanism of zeolite A nanocrystal growth from colloids at room temperature, Sci. (1979) 283 (1999) 958–960, https://doi.org/10.1126/science.283.5404.958.
[28] J. Hedlund, B. Schoeman, J. Sterte, Ultrathin oriented zeolite LTA films, Chem. Commun. (1997) 1193–1194, https://doi.org/10.1039/a702616a.
[29] W. Fan, S. Shirato, F. Gao, M. Ogura, T. Okubo, Phase selection of FAU and LTA zeolites by controlling synthesis parameters, Microporous Mesoporous Mater. 89 (2006) 227–234, https://doi.org/10.1016/j.micromeso.2005.11.001.
[30] W. Fan, F. Meneau, W. Bras, M. Ogura, G. Sankar, T. Okubo, Effects of silicon sources on the formation of nanosized LTA: an in situ small angle X-ray scattering and wide angle X-ray scattering study, Microporous Mesoporous Mater. 101 (2007) 134–141, https://doi.org/10.1016/j.micromeso.2006.10.007.
[31] P.S. Singh, V.K. Aswal, S.G. Chaudhri, W. Schwieger, Structural evolution during nucleation of Si-rich LTA nanocrystals from colloidal solution, Microporous Mesoporous Mater. 259 (2018) 99–110, https://doi.org/10.1016/j.micromeso.2017.10.006.

[32] J. Zhang, W. Yan, H. Ding, Y. Liu, K. Tang, J. Yu, R. Xu, Microemulsion-directed synthesis of zeolite A nano-crystals, Stud. Surf. Sci. Catal. 170 (2007) 475–479, https://doi.org/10.1016/S0167-2991(07)80879-2.
[33] M. Maldonado, M.D. Oleksiak, S. Chinta, J.D. Rimer, Controlling crystal polymorphism in organic-free synthesis of Na-zeolites, J. Am. Chem. Soc. 135 (2013) 2641–2652, https://doi.org/10.1021/ja3105939.
[34] C.F. Macrae, I. Sovago, S.J. Cottrell, P.T.A. Galek, P. McCabe, E. Pidcock, M. Platings, G.P. Shields, J.S. Stevens, M. Towler, P.A. Wood, *Mercury 4.0*: from visualization to analysis, design and prediction, J. Appl. Crystallogr. 53 (2020) 226–235, https://doi.org/10.1107/S1600576719014092.
[35] G. Garcia, S. Cabrera, J. Hedlund, J. Mouzon, Selective synthesis of FAU-type zeolites, J. Cryst. Growth 489 (2018) 36–41, https://doi.org/10.1016/j.jcrysgro.2018.02.022.
[36] C. Chatelard, R.Martinez Franco, M. Dodin, A. Tuel, Seed-assisted crystallization of high-silica cubic and hexagonal faujasite polymorphs in the presence of the tetraethylammonium (TEA^+) cation, CrystEngComm. 26 (2024) 4073–4081, https://doi.org/10.1039/D4CE00257A.
[37] Y. Huang, J. Yao, X. Zhang, C. Kong, H. Chen, D. Liu, M. Tsapatsis, M.R. Hill, A. J. Hill, H. Wang, Role of ethanol in sodalite crystallization in an ethanol–Na_2O–Al_2O_3–SiO_2–H_2O system, CrystEngComm. 13 (2011) 4714–4722, https://doi.org/10.1039/c1ce05194f.
[38] Y. Zhan, X. Li, Y. Zhang, L. Han, Y. Chen, Phase and morphology control of LTA/FAU zeolites by adding trace amounts of inorganic ions, Ceram. Int. 39 (2013) 5997–6003, https://doi.org/10.1016/j.ceramint.2013.01.005.
[39] Z. Mi, S. Li, W. Liu, J. Wang, D. Deng, P. Liu, P. Tian, C. Liu, W. Yan, K. Zhu, Z. Wang, Z. Liu, J. Yu, Direct synthesis of highly siliceous faujasite-type zeolite enabled by low charge density organic structure-directing agents, J. Am. Chem. Soc. 147 (2025) 16922–16934, https://doi.org/10.1021/jacs.4c18522.
[40] C.S. Cundy, P.A. Cox, The hydrothermal synthesis of zeolites: precursors, intermediates and reaction mechanism, Microporous Mesoporous Mater. 82 (2005) 1–78, https://doi.org/10.1016/j.micromeso.2005.02.016.
[41] S. Alfaro, C. Rodríguez, M.A. Valenzuela, P. Bosch, Aging time effect on the synthesis of small crystal LTA zeolites in the absence of organic template, Mater. Lett. 61 (2007) 4655–4658, https://doi.org/10.1016/j.matlet.2007.03.009.
[42] A. Corma, F. Rey, J. Rius, M.J. Sabater, S. Valencia, Supramolecular self-assembled molecules as organic directing agent for synthesis of zeolites, Nature 431 (2004) 287–290, https://doi.org/10.1038/nature02909.
[43] L.B. McCusker, D.H. Olson, C. Baerlocher, Atlas of Zeolite Framework Types, Elsevier, 2007, https://doi.org/10.1016/B978-0-444-53064-6.X5186-X.
[44] S. Turner, J.R. Sieber, T.W. Vetter, R. Zeisler, A.F. Marlow, M.G. Moreno-Ramirez, M.E. Davis, G.J. Kennedy, W.G. Borghard, S. Yang, A. Navrotsky, B.H. Toby, J. F. Kelly, R.A. Fletcher, E.S. Windsor, J.R. Verkouteren, S.D. Leigh, Characterization of chemical properties, unit cell parameters and particle size distribution of three zeolite reference materials: RM 8850 – zeolite Y, RM 8851 – zeolite A and RM 8852 – ammonium ZSM-5 zeolite, Microporous Mesoporous Mater. 107 (2008) 252–267, https://doi.org/10.1016/j.micromeso.2007.03.019.
[45] C.F. Holder, R.E. Schaak, Tutorial on powder X-ray diffraction for characterizing nanoscale materials, ACS Nano 13 (2019) 7359–7365, https://doi.org/10.1021/acsnano.9b05157.
[46] G. Ye, Y. Sun, Z. Guo, K. Zhu, H. Liu, X. Zhou, M.-O. Coppens, Effects of zeolite particle size and internal grain boundaries on Pt/beta catalyzed isomerization of n-pentane, J. Catal. 360 (2018) 152–159, https://doi.org/10.1016/j.jcat.2018.01.033.
[47] F. Babick, Dynamic Light Scattering (DLS), in: Characterization of Nanoparticles, Elsevier, 2020, pp. 137–172, https://doi.org/10.1016/B978-0-12-814182-3.00010-9.
[48] J. García-Martínez, D. Cazorla-Amorós, A. Linares-Solano, Further evidences of the usefulness of CO_2 adsorption to characterize microporous solids, Stud. Surf. Sci. Catal. 128 (2000) 485–494, https://doi.org/10.1016/S0167-2991(00)80054-3.
[49] L. Güemes, M. Navarro, F. Cacho-Bailo, C.D. Jaimes-Paez, D. Cazorla-Amorós, C. Téllez, J. Coronas, Zeolite@metal-organic framework core-shell synthesized from the aluminum of the zeolite with accessible internal surface for CO_2 adsorption, Chem. Eng. J. 518 (2025) 164314, https://doi.org/10.1016/j.cej.2025.164314.
[50] M. Thommes, K. Kaneko, A.V. Neimark, J.P. Olivier, F. Rodriguez-Reinoso, J. Rouquerol, K.S.W. Sing, Physisorption of gases, with special reference to the evaluation of surface area and pore size distribution (IUPAC Technical Report), Pure Appl. Chem. 87 (2015) 1051–1069, https://doi.org/10.1515/pac-2014-1117.
[51] Y.-S. Bae, A.Ö. Yazaydın, R.Q. Snurr, Evaluation of the BET method for determining surface areas of MOFs and zeolites that contain ultra-micropores, Langmuir 26 (2010) 5475–5483, https://doi.org/10.1021/la100449z.
[52] T. Montanari, E. Finocchio, E. Salvatore, G. Garuti, A. Giordano, C. Pistarino, G. Busca, CO_2 separation and landfill biogas upgrading: a comparison of 4A and 13X zeolite adsorbents, Energy 36 (2011) 314–319, https://doi.org/10.1016/j.energy.2010.10.038.
[53] E. Khoramzadeh, M. Mofarahi, C.-H. Lee, Equilibrium adsorption study of CO_2 and N_2 on synthesized zeolites 13X, 4A, 5A, and beta, J. Chem. Eng. Data 64 (2019) 5648–5664, https://doi.org/10.1021/acs.jced.9b00690.
[54] L. Hauchhum, P. Mahanta, Carbon dioxide adsorption on zeolites and activated carbon by pressure swing adsorption in a fixed bed, Int. J. Energy Environ. Eng. 5 (2014) 349–356, https://doi.org/10.1007/s40095-014-0131-3.